

## The difference in the type of zinc oxide nanostructures depending on the growth layer

S. A. H. Abbas<sup>a</sup>, E. S. Hassan<sup>b</sup>, O. M. Abdulmunem<sup>b,\*</sup>

<sup>a</sup>Ministry of Education, Directorate General for Education, Iraq, Baghdad

<sup>b</sup>Physics department, college of science, Mustansiriyah University, Baghdad-Iraq

In this study, RF-sputtering was used to hydrothermally produce zinc oxide nanorods (ZnO NRs) on the seed layer of ZnO/Glass substrates. at different thicknesses ( $t_1 = 1135$  nm,  $t_2 = 1306$  nm,  $t_3 = 1437$  nm,  $t_4 = 1533$  nm). The structural properties were studied by X-ray diffraction, which showed that ZnO NRs and the seed layer films are polycrystalline with the same preferred reflection for the (002) plane, and the grain size of the seed layer ranges between 19.51 nm and 30.45 nm for thicknesses  $t_1$  and  $t_4$ , respectively. The measurements of the FESEM showed aspect ratios for ZnO NRs ranging from 3.03 for  $t_1$  to 4.9 for  $t_4$ , with growth in different shapes: ZnO NR rods for  $t_1$ , flowers and rod-like shapes for thicknesses of  $t_2$  and  $t_3$ , and hexagonal-rod-like shapes in  $t_4$ . Optical measurements showed a decrease in the transmittance and an increase in the energy gap values with increasing thickness.

(Received April 8, 2023; Accepted July 5, 2023)

**Keywords:** ZnO nanorods, RF sputtering, Hydrothermal method, Seed layer, Growth mechanism, Hexagonal nanostructures.

### 1. Introduction

Over the last few decades, 1D nanostructures (nanorods, nanowires, nanobelts) have received attention due to their importance and wide range of applications. ZnO is one of the best oxide semiconductors due to its ideal properties such as a wide band gap of 3.36 eV, a high exciton energy of 60 eV at room temperature that provides high thermal and chemical stability, and transparency, as well as being environmentally friendly. Many applications, such as blue-green optoelectronic devices and short-wavelength UV lasers, are possible for it. [1], conductive oxides, antistatic coatings, sensors, touch display panels and high-band-gap optoelectronic devices [2, 3].

ZnO 1D Due to their significant potential in gas sensing applications, particularly because of their high surface-to-volume ratio, nanostructures like nanowires, nanobelts, and nanorods have received a lot of interest. [4-6]. ZnO nanostructures have been produced using a number of different synthesis methods, including thermal evaporation Due to its distinct benefits, the hydrothermal technique has received a lot of attention. It is an easy, low-temperature (60–100°C), high-yield, and more regulated process., hydrothermal synthesis, sputtering, pulsed laser deposition, and molecular beam epitaxy [3, 7]. The hydrothermal method has attracted considerable attention because of its unique advantages: it is a simple, low-temperature (60–100°C), high-yield and more controllable process [8-10].

There are several ways to synthesize 1D ZnO. For ZnO nanorods (ZNRs) in particular, the vapor phase and wet phase both has advantages and disadvantages. The vapor phase method requires high temperatures, up to 900 °C and not all materials used as substrates are suitable. Liquid phase or chemical methods, including hydrothermal methods, are usually easy and inexpensive but accompanied by defects such as treatment by annealing. In a study by *Cao P. et al.* [11], vertically aligned ZnO-NRs were synthesized to provide C<sub>2</sub>H<sub>5</sub>OH sensors with good response repeatability. *Sonalika et al.* [12] studied the flower and nanorod assembly of ZnO nanostructures that were fabricated by a hydrothermal method to study morphology-dependent gas-sensing properties. *Abdulmunem et al.* [13] studied optical characterization of ZnO doped by Al.

In this study, we focus on the difference in the thickness of the seed layer on the growth nano-hexagonal structure for suitable applications such as photoconductivity or gas sensors, where the hexagonal geometry of the nanorods is ideal for field emission [14]. It is believed that zinc oxide nanorods have superior performance in the field of detectors and sensors, so we will employ hexagonal nanostructures.

\* Corresponding author: munem@uomustansiriyah.edu.iq

<https://doi.org/10.15251/DJNB.2023.183.793>

## 2. Experimental part

In the first stage, a seed layer of zinc oxide was deposited on glass substrates using the RF magnetron sputtering method, with the deposition conditions listed in Table 1. Four models of ZnO were obtained on glass substrates of varying thickness:  $t_1=1135$  nm,  $t_2=1306$  nm,  $t_3=1437$  nm,  $t_4=1533$  nm. The resulting sample was then annealed at  $450^\circ\text{C}$  for 1 h at atmospheric pressure in a stainless-steel furnace (304 grade and exterior). The structural and surface roughness were examined by XRD (DJ-3500 X-ray diffractometer) and FESEM (Field Emission Scanning Electron Microscope and Energy Dispersive X-ray Spectrometer, FESEM-EDS 7610F). The growth solution was prepared by adding 1.8 mL of ammonia (Thomas Baker 29%  $\text{NH}_3$ ) to 80 mL of deionized water (BI Supply Deionized Water) to obtain a pH of 11, which was calculated by a LCD Digital pH Meter (accuracy: 0.01, operating temperature:  $60^\circ\text{C}$ ).  $[\text{ZnO}(\text{NO}_3)_2 \cdot 6\text{H}_2\text{O}]$  (PIOCHEM) zinc nitrate with molar mass (183.48 g/mol) at 99.99% purity was added to the growth solution to obtain molarity  $M = 0.028$  mol/L. The solution was carried out by a magnetic stirrer at room temperature ( $25$  to  $30^\circ\text{C}$ ) for 15 min. The ZnO seed layer was horizontally fixed in a Teflon holder as shown in Figure 1, with the zinc oxide seed layer facing down, such that the samples were immersed in the growing liquid. Then the Teflon cell was transferred to a stainless-steel autoclave (200 mL capacity), and it was closed tightly and placed in an oven at a temperature of  $90^\circ\text{C}$  for 3 h, after which the samples were taken out and left to cool down.

Table 1. RF sputter deposition parameter of seed layers.

Substrate	Solid-lime glass ( $2.5 \times 7 \times 1$ ) mm
Target	ZnO ( $50 \times 3$ ) mm
Gas	Argon
Base Pressure	$2.15 \times 10^{-5}$ torr
Substrate Rotate Speed	5 cyc /min
Substrate To Target Distance	30 cm
Substrate Temperature	$25 - 27^\circ\text{C}$
rf Power	100 w
Sputtering Pressure	$1.72 \times 10^{-2}$ torr
Deposition Rate	2.42 nm/min

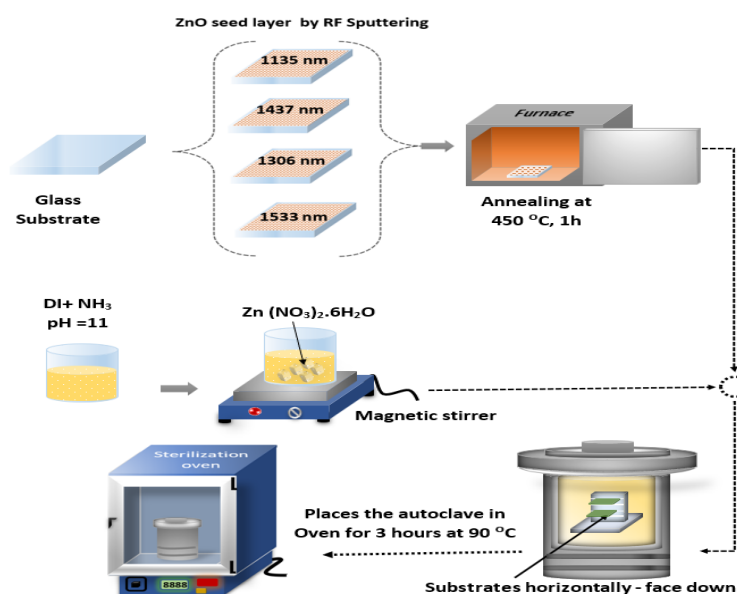


Fig. 1. Illustration of the hydrothermal system with the stainless-steel autoclave inside the oven.

### 3. Result and discussion

Figure 2 display the X-ray diffraction pattern of a ZnO seed layer deposited on a glass substrate prepared by RF magnetron sputtering with different thicknesses ( $t_1=1135$  nm,  $t_2=1306$  nm,  $t_3=1437$  nm,  $t_4=1533$  nm) and annealed at 450 °C for 1 h, which illustrates that it consists of hexagonal polycrystalline ZnO with fine peaks along the (002) plane associated with diffraction angle  $2\theta = 34.5^\circ$  and with minor reflections (100), (101), (102), (110), (103) and (200) associated with diffraction angles  $2\theta = 31.9^\circ, 36.4^\circ, 47.7^\circ, 56.6^\circ, 62.8^\circ$  and  $66.28^\circ$ . The diffraction intensity of the ZnO (002) peak increases as the thickness increases due to more crystallites growing in the structure. The lattice constants calculated for the (002) plane by using Equation 1 and listed in Table 2 are both theoretical and calculated values that show high convergence.

Equations 2, 3 and 4 [14-16] were used to calculate crystallite size, microstrain, and dislocation density respectively, which are listed in Table 2. We found that the crystallite size increases with increasing thickness, and that an increase in the period (deposition time) of RF-sputtering allows the ZnO particles to have more kinetic energy, which helps them to aggregate into larger granules [1]. The decreases in Microstrain and dislocation density this is due to the improvement in the crystalline properties and thus the reduction of crystalline defects [17].

$$\frac{1}{d^2} = \frac{4}{3} \left[ \frac{h^2+hk+k^2}{a^2} \right] + \frac{l^2}{c^2} \quad (1)$$

$$D = \frac{k\lambda}{\beta \cos\theta} \quad (2)$$

$$\varepsilon = \frac{\beta \cos\theta}{4} \quad (3)$$

$$\delta = \frac{1}{D^2} \quad (4)$$

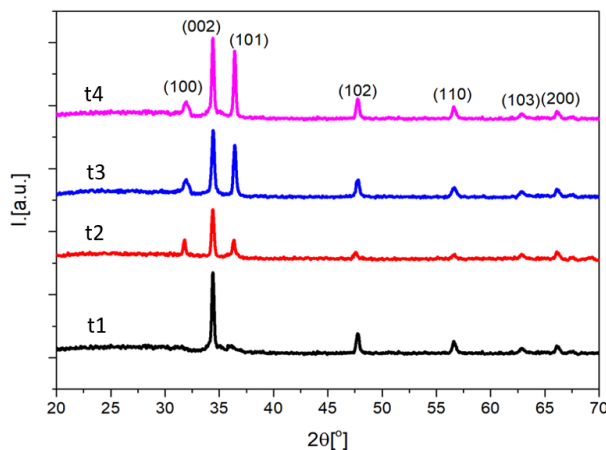


Fig. 2. X-ray diffraction for ZnO samples deposited by RF magnetron sputtering.

Table 2. Structural parameters for ZnO seed layer prepared by RF- Sputtering.

Sa.	$2\theta$ [°]	(hkl)	lattice constant [Å]				crystallite size [nm]	Macrostrain $\times 10^{-5}$	Dislocation density $\times 10^{-5}$ [1/m <sup>2</sup> ]
			Observed		JCPDS				
			a	c	a	c			
t <sub>1</sub>	34.5	(002)	3.240	5.208	3.249	5.206	19.51	58.54	26.10
t <sub>2</sub>	34.5	(002)	3.240	5.208	3.249	5.206	20.05	58.43	24.69
t <sub>3</sub>	34.5	(002)	3.240	5.208	3.249	5.206	25.14	45.42	15.72
t <sub>4</sub>	34.5	(002)	3.240	5.208	3.249	5.206	30.45	37.50	10.71

Figure 3 displays the FESEM images of ZnO seed layer nanoparticles, including a top view at a 500 nm scale and a cross-section at a 2  $\mu\text{m}$  scale. Figures (3-a1 and 3-a2) show the first sample  $t_1=1135\text{nm}$ , where the surface topography shows that the particles are heterogeneous in terms of size and distribution, and the average particle size is about 20.23 nm, as shown in figure (4-a), which represents the average distribution of particle radii as a function of their number, calculated by the ImageJ software.

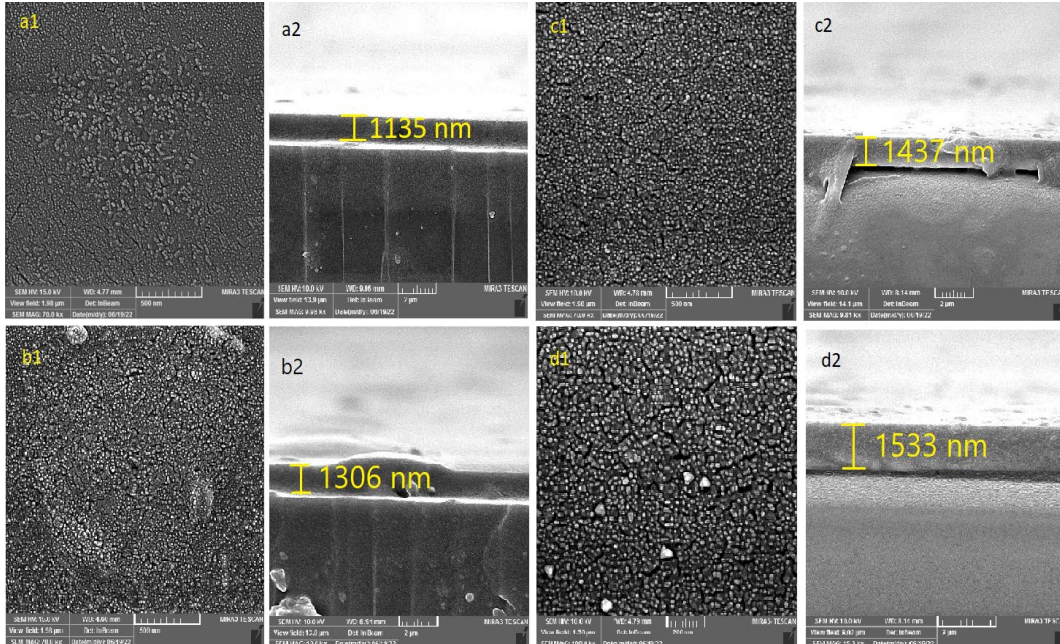


Fig. 3. Shown FESEM images for all ZnO samples deposited by RF magnetron sputtering.

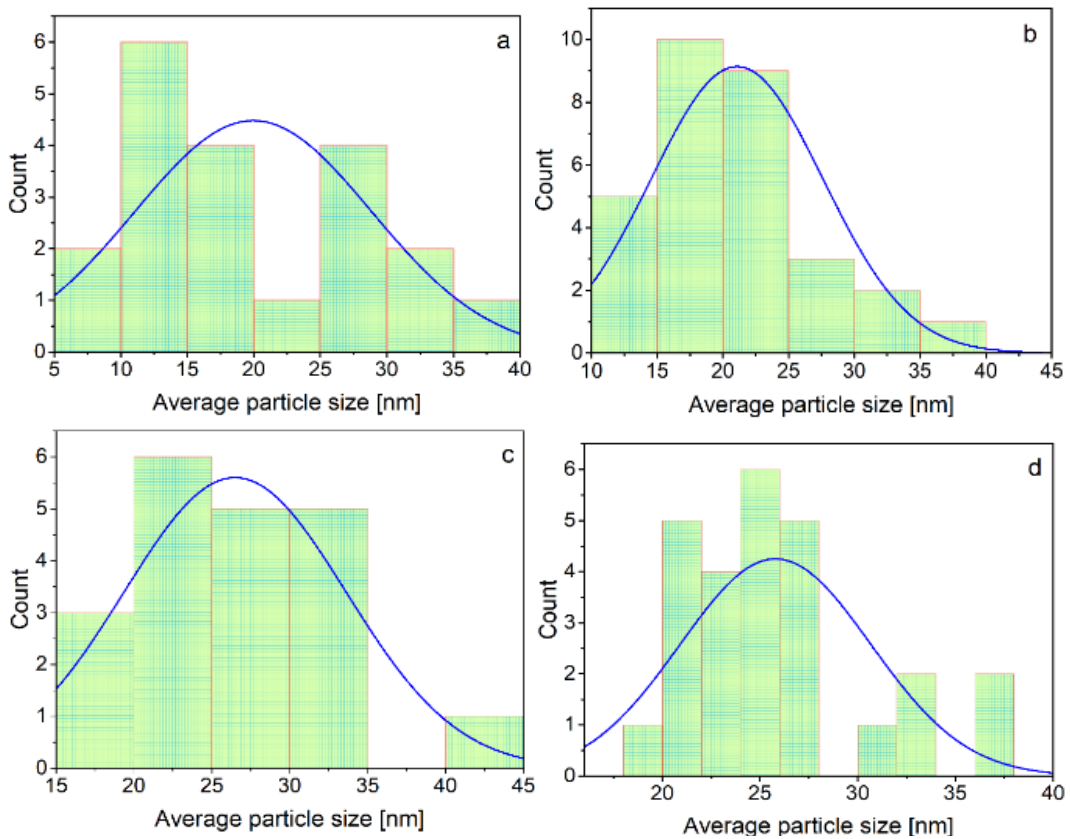


Fig. 4. Gaussian distribution of ZnO nanoparticles seed layers (a)  $t_1$ , (b)  $t_2$ , (c)  $t_3$  and (d)  $t_4$ .

At the second thickness of  $t_2=1306$  nm, we observed in Figures (3- b1 and 3-b2) that the distribution of zinc oxide particles nanoparticles became more uniform and denser compared to  $t_1$ , and that the average particle size increased to 23.82 nm, as shown in Figure (4-b). Figures (3-c1 and 3-c2) and (3-d1 and 3-d2) show thickness  $t_3=1437$  nm and  $t_4=1533$  nm, for which particles on the surface of the samples are found to be denser density and more evenly distributed, with the average particle size increasing to 26.09 nm for  $t_3$  and 26.98 nm for  $t_4$  as shown in Figures (4-c and 4-d). Thus, the observed particle size of the FESEM images is in good concurrence with the crystallite size values from the XRD measurement.

Figure 5 represents the X-ray diffraction pattern of zinc oxide NR growth on glass/ZnO seed layers with varying thickness by the hydrothermal method. The diffraction pattern for all models is polycrystalline with the samples having a wurtzite ZnO structure according to the JCPDS 36-1451 card. The dominant reflection is the (002) plane at angle  $2\theta = 34.42^\circ$  for all samples. One of the characteristics is the growth on the (002) level. A mechanism which is often put forward to explain the formation of oriented grains is that during nucleation the total energy of the forming clusters is at a minimum if the boundary surface has the lowest possible surface free energy [17]. The crystallite size of the (002) plan of the prepared samples was estimated from line broadening using the Scherrer equation (1) [18] and listed in Table (3), along with the crystallite size increase as well as the intensity. This enhancement in XRD peak intensities suggest that thickness of the seed layer induces the atoms to find proper lattice sites and plays an important role in increasing the XRD peak intensities, which induces crystallinity improvement of the grown ZnO films, which can indicate crystallite enhancement in agreement with *Anton et al* [19]. On the other hand, we calculate both microstrain and dislocation density, finding a decrease in values with increasing thickness as illustrated in table 3. There are several secondary reflections (100), (101), (102), (110) and (103) at associated angles  $31.86^\circ$ ,  $36.37^\circ$ ,  $47.84^\circ$ ,  $56.67^\circ$  and  $62.95^\circ$  as illustrated in Figure (5). This result agrees with the JCPDS 36-1451 card, as well as with *P. Rajasekaran et al.* [20]. Table (3) includes all results that we obtained compared with standard values of the card JCPDS.

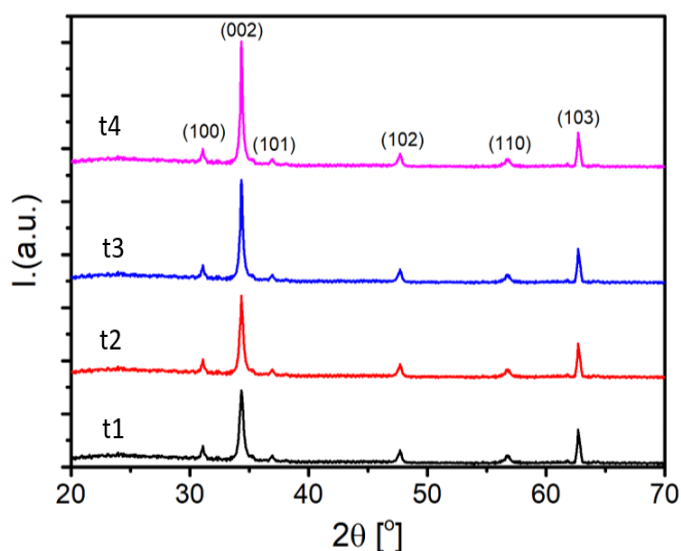


Fig. 5. Represents X-ray diffraction pattern of zinc oxide NR growth on glass/ZnO seed layers with varying thickness by the hydrothermal method.

Table 3. Structural parameters for ZnO nanostructure growth by hydrothermal method.

Sa.	2 $\theta$ [°]	(hkl)	lattice constant [Å]				crystallite size [nm]	Macrostrain $\times 10^{-5}$	Dislocation density $\times 10^{-5}$ [1/m <sup>2</sup> ]
			Observed		JCPDS				
			a	c	a	c			
t <sub>1</sub>	34.5	(002)	3.251	5.231	3.249	5.206	31.86	11.37	9.84
t <sub>2</sub>	34.5	(002)	3.251	5.231	3.249	5.206	32.46	11.161	9.49
t <sub>3</sub>	34.5	(002)	3.251	5.231	3.249	5.206	34.65	10.45	8.32
t <sub>4</sub>	34.5	(002)	3.251	5.231	3.249	5.206	37.82	9.57	6.989

Figures (6-a, 6-b and 6-c) show the typical FESEM images of ZnO NRs prepared by the hydrothermal method on a ZnO/glass substrate, denoted by t<sub>1</sub>. The nanorods were prepared by the RF magnetron sputtering method, and the average particle size of seed layer is 20.23 nm. It is clear from FESEM images in Figures (6-a, 6-b and 6-c) that the growth of nanostructures was rod-like, dense, and perpendicular to the substrate surface with diameter ranges between 152 to 27 nm and length ranges between 628 to 187 nm. Figures (6-d, 6-e and 6-f) show FESEM images of ZnO NR growth on the t<sub>2</sub> substrate with an average particle size in the seed layer of 20.82 nm. The rods in Figure (6-a, 6-b and 6-c) aggregate to form flowers consisting of a flower base of ZnO NRs parallel to the substrate surface with high density and irregular hexagonal shapes, with length ranging from 500 to 754 nm and diameter ranging from 80 to 120 nm. On these flower bases grow vertical floral shapes of ZnO NRs that take hexagonally packed shapes, with diameters ranging from 45 to 96 nm. The transition from rod-like to flower-like ZnO NRs is likely attributable to the Gaussian distribution of nucleation sites, as illustrated in Figure (4). Figures (6-g, 6-h and 6-i) represent a substrate of thickness t<sub>3</sub> with an average particle size in the seed layer of 26.09 nm and where the floral shapes in the substrate of thickness t<sub>2</sub> have turned into spherical shapes, consisting of irregular hexagonal ZnO NRs with a diameter of 35–70 nm. At this stage, we notice the disappearance of the flower base, which was formed on the thickness t<sub>2</sub> substrate. The images in Figure (6-j, 6-k and 6-l) represent the substrate of t<sub>4</sub>, where the average particle size of the seed layer is 26.98 nm, the growth has a homogeneous distribute with good alignment and uniform perpendicular growth on the substrate surface, and the average diameter and average length are 117 nm and 628.5 nm, respectively.

To explain the growth mechanism of different nanostructure types for the wurtzite ZnO crystal, we note that it has two polar planes: six crystallographic ally equivalent nonpolar planes parallel to the c-axis, which are more stable because of their comparatively low surface energy, and low-index planes with high surface energy [21]. The formation of various shapes of ZnO nanocrystals originates in the relative growth rates of different crystal facets. There is a large difference in the growth rates of the wurtzite hexagonal ZnO crystals in different directions under hydrothermal conditions [22]. According to the lowest energy principle, hexagonal ZnO crystals are inclined to grow along the [001] facet to achieve surface energy minimization, hence the growth velocity along the [001] direction is faster than other growth facets, which leads to the formation of nanorods along the c-axis. The growth rate  $V$  is shown to slow down in the order that  $V(001) > V(01\bar{1}) > V(010) > V(011) > V(00\bar{1})$  [23], as shown in Figure (7). We explain the growth process by proposing that crystal growth is mediated by growth formation of the units that are proposed to be  $Zn(OH)_4^{2-}$ , called “coordination polyhedral.” These units can form clusters that precipitate when a critical size is reached [23]. When we applied the previous calculations to the length and diameter of the rods growing on the ZnO seed layers and compared with their thickness, we noticed that the aspect ratio increases with increasing thickness, as shown in Figure 8. This ratio increased from 3.03 nm to 4.9 at t<sub>4</sub>, which provides a high surface area and thus allows for a wide range of applications.

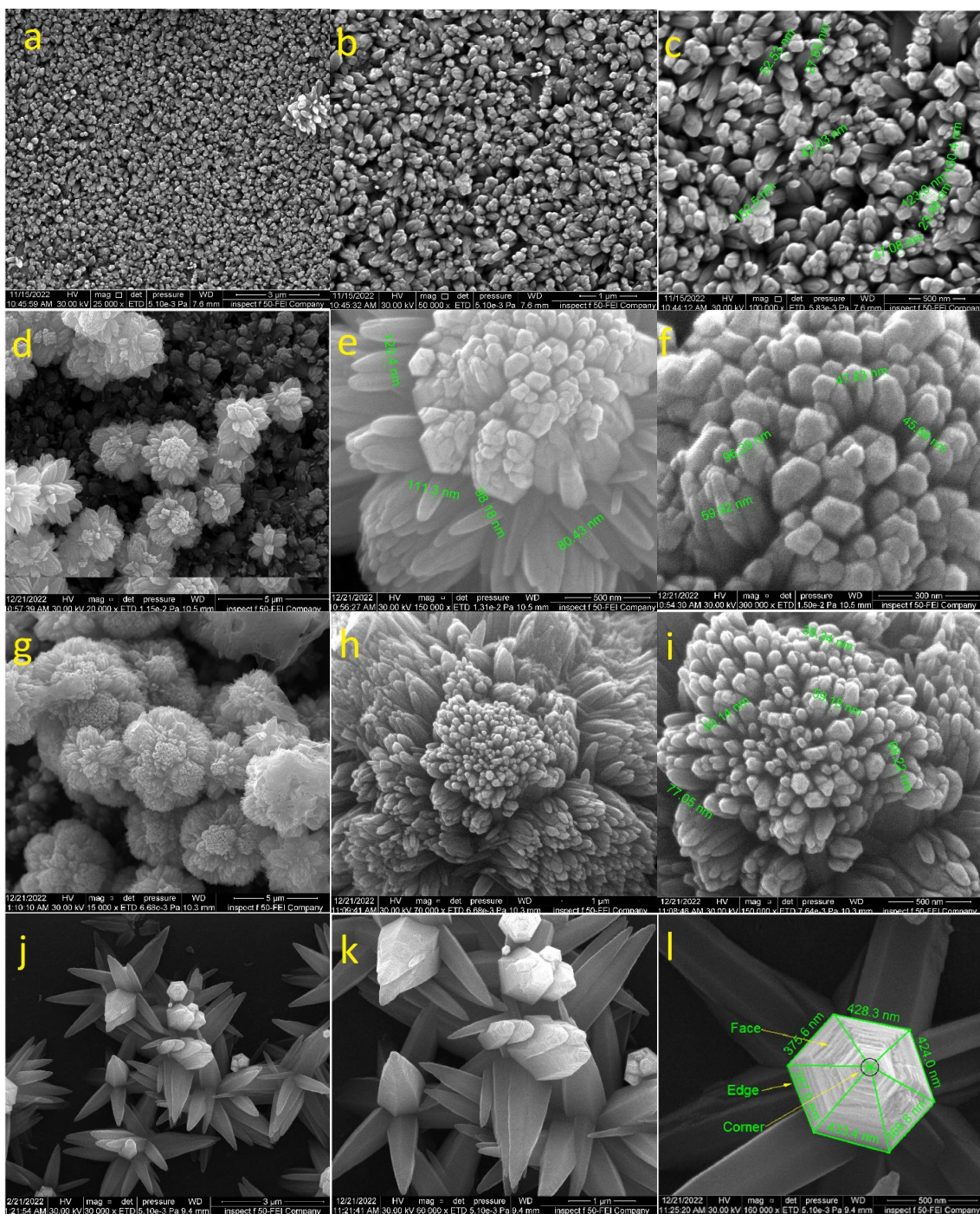


Fig. 6. Shows FESEM images for ZnO nanorods growth by hydrothermal method.

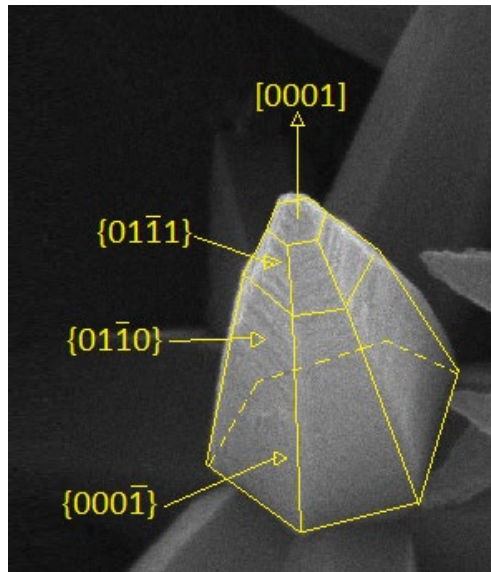


Fig. 7. Illustrated the crystal growth facets according to their growth speed.

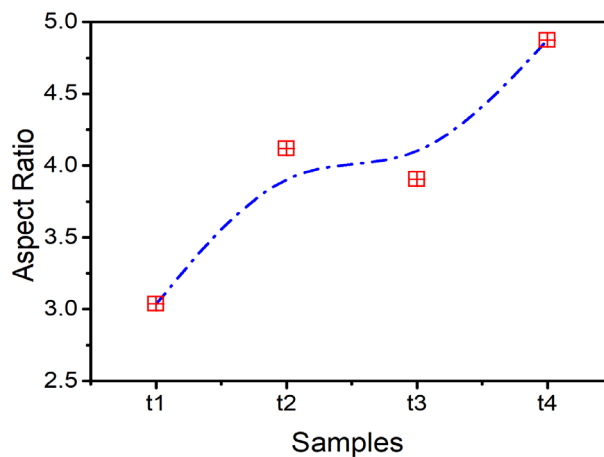


Fig. 8. Illustrate increasing of aspect ratio for growth rods with increasing thickness ZnO seed layer.

Figure 9 depicts the transmittance spectrum of ZnO nanostructure samples prepared by the hydrothermal method and with layers of ZnO of various thicknesses seed deposited on glass substrates as a function of wavelength. Figure 9 shows the decrease in transmittance with changes in both the thickness and the different nanostructures. According to the optical characteristics of the ZnO semiconductor in the UV-visible region, all films exhibit increases in transmittance at wavelengths longer than 400 nm. [1], which is confined to Vis and the near IR. In figure 10 the relationship between  $(\alpha h\nu)^2$  and the photon energy ( $h\nu$ ), where the value of the energy gap can be calculated by extrapolating the linear portion of the curve and setting the value of the magnitude  $(\alpha h\nu)^2 = 0$ , as in the equation (5) [24]. The energy gap increases from 3.18 eV to 3.31 eV as the thickness increases from 1135 to 1533 nm.

$$(\alpha h\nu)^2 = B(h\nu - E_g^{opt})^r \quad (5)$$

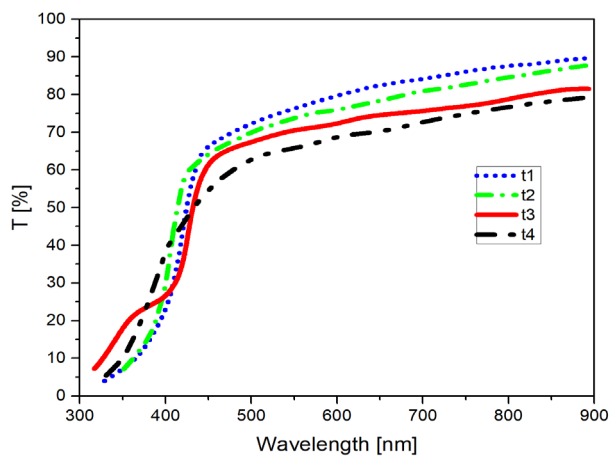


Fig. 9. Represents the transmittance spectrum as a function of the wavelength of the ZnO Nanostructure synthesized by hydrothermal method.

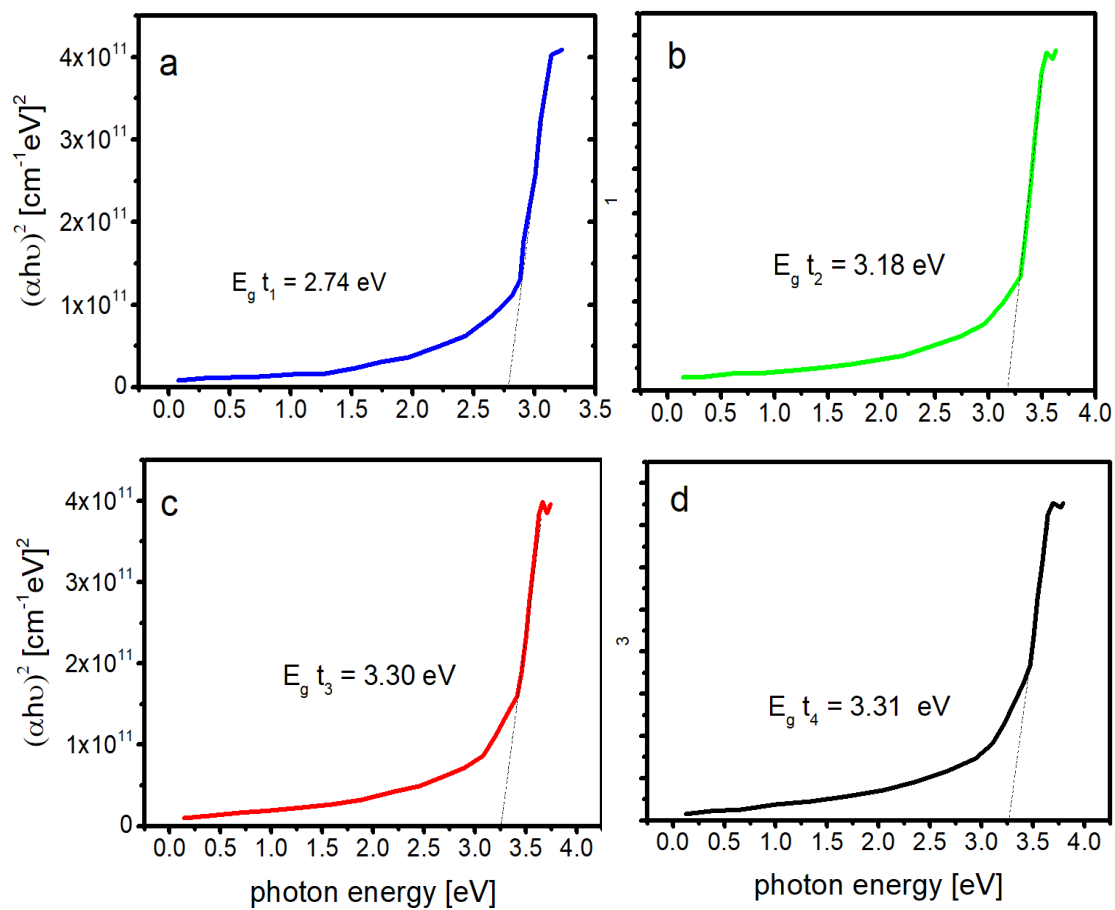


Fig. 10. Shown the  $(\alpha h\nu)^2$  as a function of the photon energy of the ZnO nanostructure.

#### 4. Conclusions

In this research, the effect of the thick layers of zinc oxide deposited by the PVD on the nanostructure produced by the hydrothermal method was studied. The changes nucleation site and particle size were examined.  $t_1$  thickness nanostructures were rod-like, dense, and perpendicular to the substrate surface with diameter ranges between 152 to 27 nm and length ranges between 628 to 187 nm. the  $t_2$  aggregate forms flowers grow vertical floral shapes of ZnO NRs that take hexagonally packed shapes, with diameters ranging from 45 to 96 nm.  $t_3$  spherical shapes, consisting of irregular hexagonal ZnO NRs with a diameter of 35 to 70 nm.  $t_4$  the growth has a homogeneous distribute with good alignment and uniform perpendicular growth on the substrate surface, and the average diameter and average length are 117 nm and 628.5 nm, respectively. And one of the most important conclusions is aspect ratio increases with increasing growth layer thickness.

#### Acknowledgements

The authors would like to express their gratitude and acknowledge the department of physics staff at college of science of the Mustansiriyah University, the Laboratory of Advanced Materials, for making the necessary measurements.

#### References

- [1] J.K.Lee, G.J.Sun, W.S. Lee, S.K.Hyun, K.K. Kim, S.B.Choi, and C.Lee, Scientific Reports, 7(1), p.13034, (2017); <https://doi.org/10.1038/s41598-017-13556-0>
- [2] C.-T. Lee, Materials, vol. 3, no. 4, pp. 2218-2259, (2010); <https://doi.org/10.3390/ma3042218>
- [3] E.S. Hassan, and O.M. Abdulmunem, Brazilian Journal of Physics, 52(5), p.160, (2022); <https://doi.org/10.1007/s13538-022-01158-9>
- [4] N. Kaur, M. Singh, and E. Comini, Langmuir, vol. 36, no. 23, pp. 6326-6344, (2020); <https://doi.org/10.1021/acs.langmuir.0c00701>
- [5] H.M. Mikhlif, , M.O.Dawood, O.M. Abdulmunem, and M.K. Mejbil, Acta Physica Polonica, A., 140(4), (2021); <https://doi.org/10.12693/APhysPolA.140.320>
- [6] T. Zhou and T. Zhang, Small Methods, vol. 5, no. 9, p. 2100515, (2021); <https://doi.org/10.1002/smt.202100515>
- [7] R. Saravanan, E. Thirumal, V. Gupta, V. Narayanan, and A. Stephen, Journal of Molecular Liquids, vol. 177, pp. 394-401, (2013); <https://doi.org/10.1016/j.molliq.2012.10.018>
- [8] B. Liu and H. C. Zeng, Journal of the American Chemical Society, vol. 125, no. 15, pp. 4430-4431, (2003); <https://doi.org/10.1021/ja0299452>
- [9] Z. Qiu, K. Wong, M. Wu, W. Lin, and H. Xu, Applied physics letters, vol. 84, no. 15, pp. 2739-2741, (2004); <https://doi.org/10.1063/1.1697633>
- [10] W. Shi, S. Song, and H. Zhang, Chemical Society Reviews, vol. 42, no. 13, pp. 5714-5743, (2013); <https://doi.org/10.1039/c3cs60012b>
- [11] P. Cao et al., Sensors and Actuators B: Chemical, vol. 298, (2019); <https://doi.org/10.1016/j.snb.2019.126850>
- [12] S. Agarwal et al., Sensors and Actuators B: Chemical, vol. 292, pp. 24-31, (2019); <https://doi.org/10.1016/j.snb.2019.04.083>
- [13] O. M. Abdulmunem, M. J. M. Ali, and E. S. Hassan, Optical Materials, vol. 109, p. 110374, (2020); <https://doi.org/10.1016/j.optmat.2020.110374>
- [14] Z. L. Wang, Journal of physics: condensed matter, vol. 16, no. 25, p. R829, (2004); <https://doi.org/10.1088/0953-8984/16/25/R01>

- [15] A. S. Rini, Y. Rati, A. A. Umar, and N. A. Abdullah, *International Journal of Nanoelectronics & Materials*, vol. 13, (2020).
- [16] M. K. Kamil and K. A. Jasim, *IOP Conference Series: Materials Science and Engineering*, vol. 928, no. 7: IOP Publishing, p. 072109, (2020); <https://doi.org/10.1088/1757-899X/928/7/072109>
- [17] F. Guo et al., *Nature nanotechnology*, vol. 7, no. 12, pp. 798-802, (2012); <https://doi.org/10.1038/nnano.2012.187>
- [18] B. Fultz, J. Howe, B. Fultz, and J. Howe, *Transmission Electron Microscopy and Diffractometry of Materials*, pp. 587-615, (2013); [https://doi.org/10.1007/978-3-642-29761-8\\_12](https://doi.org/10.1007/978-3-642-29761-8_12)
- [19] D. K. Aswal and S. K. Gupta, *Science and technology of chemiresistor gas sensors*. Nova Publishers, (2007).
- [20] S. Saleem et al., *Journal of Materials Research and Technology*, vol. 19, pp. 2126-2134, (2022); <https://doi.org/10.1016/j.jmrt.2022.05.190>
- [21] A. A. Bobkov et al., 2018 IEEE International Conference on Electrical Engineering and Photonics (EExPolytech): IEEE, pp. 219-221, (2018); <https://doi.org/10.1109/EExPolytech.2018.8564407>
- [22] P. Rajasekaran, H. Kannan, S. Das, M. Young, and S. Santra, *AIMS Environmental Science*, vol. 3, no. 3, pp. 439-455, (2016); <https://doi.org/10.3934/environsci.2016.3.439>
- [23] S. Goel and B. Kumar, *Journal of Alloys and Compounds*, vol. 816, p. 152491, (2020); <https://doi.org/10.1016/j.jallcom.2019.152491>
- [24] A. Das, P. M. Kumar, M. Bhagavathiachari, and R. G. Nair, *Materials Science and Engineering: B*, vol. 269, p. 115149, (2021); <https://doi.org/10.1016/j.mseb.2021.115149>
- [25] D. Köhl, *The influence of energetic bombardment on the structure formation of sputtered zinc oxide films. Development of an atomistic growth model and its application to tailor thin film properties*, (2011).
- [26] B. A. Hasan and I. H. Shallal, *Journal of Nanotechnology & Advance Materials*, vol. 2, pp. 43-49, (2014); <https://doi.org/10.12785/jnam/020201>